

High-resolution He-scattering apparatus for gas-surface interaction studies

Rudolf David, Klaus Kern, Peter Zeppenfeld, and George Comsa

Institut für Grenzflächenforschung und Vakuumphysik, Kernforschungsanlage Jülich, Postfach 1913, D-5170 Jülich, Germany

(Received 10 June 1986; accepted for publication 22 July 1986)

A high-resolution apparatus designed for the study of elastic and inelastic scattering of thermal helium atoms from crystal surfaces is presented. The highly expanded He nozzle beam has an energy spread $\Delta E/E$ of about 1.4% and is collimated to 0.2° . The angle subtended by the detector opening as seen from the sample is also 0.2° . Beam intensities as low as 10^{-6} of the specular beam intensity from a low-temperature clean Pt(111) surface are detectable. Pseudorandom chopping with a resolution of $2.5 \mu\text{s}$ (flight path 790 mm) is used for time-of-flight (TOF) analysis of the scattered helium. The base pressure in the sample chamber is in the low 10^{-11} mbar. The capabilities of the apparatus are demonstrated for physisorbed Xe adlayers on Pt(111). The results presented are obtained by using He scattering in various modes: coherent inelastic, coherent elastic, and incoherent (diffuse) elastic. This technique allows for a nondestructive nearly exhaustive characterization of the thermodynamics, structure, and dynamics of physisorbed adlayers on arbitrary substrates.

INTRODUCTION

Various experiments involving molecular beam scattering from solid surfaces have substantially contributed over the years to a better understanding of gas-surface interactions, in particular of the interaction of the beam particles themselves with crystal surfaces. On the basis of this understanding and of recent methodological and technical progress, molecular beam scattering starts to become a powerful tool for the investigation of surfaces and surface processes. It is especially the "He beam" which appears to supply rich information on structure and dynamics of clean and adsorbate covered surfaces, on the interaction of other gases and of ions with solid surfaces, etc. The information is often of a quality hardly accessible to other probes. The thermal He nozzle beam has indeed a unique status when compared to other surface probes. Being a noble gas at thermal energy it is non-destructive and sensitive only to the first surface layer; within an easily accessible nozzle temperature range (80–450 K) the He wavelength (1.09–0.46 Å) is well suited for diffraction at crystal surfaces^{1,2} and its energy (17.2–96.9 meV) allows for high-resolution measurements of energy losses and gains (phonons)³; the He diffuse scattering is very sensitive to surface disorder.⁴

Surface lattice dynamics and two-dimensional (2D) phases and phase transitions are of great interest in today's surface physics. The study of the surface dynamics of clean and adsorbate covered solid surfaces provides detailed information on the interatomic force field at the surface.⁵ This is necessary for the understanding of (a) transport phenomena at or through the surface, (b) relaxation or reconstruction of the surface, and (c) accommodation and sticking of atoms and molecules. On the other hand, the great interest in 2D systems and their phase transitions originates in the reduced dimensionality. This allows for an *ab initio* analysis of 2D solids and liquids hardly accessible in three dimensions.^{6,7}

Closely related to the structure of 2D phases is the growth of thin films. The nature of the growth mode depends largely on the properties of the first monolayer, i.e., of the 2D phase. On the other hand, the nature of the growth determines many of the characteristics of the epitaxially grown films.

We report here on a high-resolution He-scattering apparatus, allowing for detailed studies of surface phonons, of the structure of 2D physisorbed phases and their mutual transitions, on crystal growth, etc., by means of coherent inelastic, coherent elastic, and incoherent elastic scattering of thermal He beams. High resolution has here a triple meaning: energy and angular resolution as well as high signal-to-noise ratio giving the opportunity to resolve low coherent signals out of the background.

The paper is organized as follows. In Sec. I we present the constructive details of the apparatus, including beam source, crystal holder, and time-of-flight (TOF) facility. In Sec. II we illustrate the capabilities of the apparatus with examples [Xe adlayers on Pt(111)].

I. APPARATUS

A. General

The general view of the apparatus is presented in Fig. 1. The scattering geometry is fixed, namely, $\vartheta_i + \vartheta_f = 90^\circ$, where ϑ_i and ϑ_f are incident and outgoing (detector) angles, respectively. The vacuum system consists of four main units: the three-chamber nozzle beam generator, the scattering chamber (with sample manipulator, LEED, CMA-Auger, and ion gun facilities), the pseudorandom chopper chamber, and the three-chamber detector unit.

The scattering chamber and the pseudorandom-chopper unit have been used for a number of years for TOF studies of desorbing hydrogen.⁸ Both have been described in detail in Refs. 9 and 10. Here we will focus mainly on the

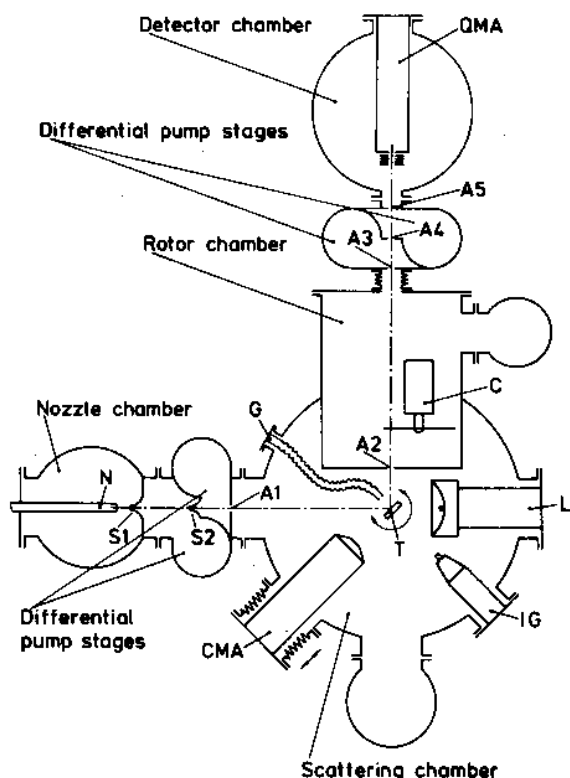


FIG. 1. Diagram (schematic) of the experimental arrangement. The scattering angle ϑ_d , i.e., the angle between the nozzle-sample and sample-detector lines, is fixed at 90° . N—nozzle beam source; S1, S2—skimmers; A1–A5—apertures; T—crystal sample; G—gas doser; CMA—Auger spectrometer; IG—ion gun; L—LEED; C—magnetically suspended pseudorandom chopper; QMA—detector, quadrupole mass analyzer with channeltron.

changes which were necessary to transform the apparatus into a high-resolution He device for surface studies. They include, in particular, the improvement of the vacuum conditions in the scattering chamber, the redesign of the crystal holder allowing for the variation and precise control of the crystal temperature in the range 25–1800 K, the improvement of the resolution of the TOF unit, the substantial reduction of the He background pressure in the detector chamber, and the mounting of a previously designed and optimized highly monochromatic He beam source.¹¹ Special care was taken to avoid sample surface contamination during measurements at low temperatures. This involved, besides base pressure in the low 10^{-11} -mbar range in the scattering chamber, the rapid cooling of the sample from the high “cleaning” to the low “measurement” temperatures and the effective purification of the He beam.

B. Nozzle beam

The three chamber nozzle beam generator and its performance have already been described in detail.¹¹ We give here only some recent modifications and essential features. The nozzle aperture diameter is now reduced from 10 to 5 μm and the 1500-l s^{-1} turbomolecular pump is boosted by

a $150\text{ m}^3\text{ h}^{-1}$ roots blower. Thus, at a nozzle stagnation pressure of 160 bar and a temperature $T_{\text{nozzle}} = 78\text{ K}$, the nozzle flow rate is $\sim 3\text{ mbar l/s}$ and the source chamber He partial pressure $2.5 \times 10^{-3}\text{ mbar}$; under these conditions collisions in the source chamber do not impair the beam characteristics. The beam divergence of 0.2° is determined by the 0.3 mm opening of the second skimmer (S2). The particle flux of a 17-meV He beam (160 bar, 78 K) impinging on the target is about $2 \times 10^{19}\text{ He atoms s}^{-1}\text{ sr}^{-1}$ with a velocity spread $\Delta v/v \approx 0.7\%$. Extra-high-purity helium (less than 3 vpm impurities), which is forced through a liquid-nitrogen-cooled 10- and $4\text{-}\mu\text{m}$ tandem sinter filter, is used in order to avoid nozzle clogging and to reduce surface contamination. The temperature of the nozzle can be varied between 10 and 800 K, i.e., the He beam energy is continuously adjustable between 2 and 170 meV.

C. Vacuum system

The nozzle beam generator is flanged via a flat valve to the scattering chamber. This chamber is described in detail in Ref. 9. The ion pump has now been replaced by a magnetically suspended turbomolecular pump (TP) (560 l/s and He compression ratio 3×10^6). Together with a 40 000 l/s titanium sublimation unit, and upon a 10-h 180°C baking procedure, the TP leads to a base pressure as low as 10^{-11} mbar . After performing the sample cleaning cycles and reaching the normal working conditions, the titanium sublimator has to be switched on usually once a day. The He partial pressure in the scattering chamber is about $2 \times 10^{-8}\text{ mbar}$ when the He beam is on and the scattering geometry $\vartheta_i \neq \vartheta_f$.

A bakeable gas inlet manifold has also been flanged on the scattering chamber. It consists of five independent leak valve inlets. The exposure of the sample surface to gas from the manifold can be performed either isotropically by increasing the pressure in the scattering chamber or by means of a gas doser in front of the sample. The latter is appropriate for gases with low sticking probability in order to avoid excessive gas loading of the entire chamber.

The vacuum system of the TOF unit has also been substantially improved in comparison with the original design.⁹ All ion pumping has been replaced by turbomolecular pumps and two differential pumping stages have been added. The chopper chamber is evacuated by a 1000 l/s TP and each of the differential pumping stages by a 150 l/s TP . The three pumps are boosted by a common 150 l/s TP in order to increase the total compression ratio. Finally, the detector chamber is evacuated by a magnetically suspended 560 l/s TP (boosted by a 50 l/s TP) and intermittently by titanium sublimation. As a result the He partial base pressure in the detector chamber is in the 10^{-15} – 10^{-16} mbar range corresponding to $\sim 30\text{ counts/s}$ at a 5-mA electron current in the ionization cage of the Extranuclear quadrupole mass spectrometer. This figure is to be compared with the $2 \times 10^7\text{ counts/s}$, representing the signal of a 17-meV He beam specularly reflected ($\vartheta_i = \vartheta_f = 45^\circ$) from a clean Pt(111) surface at 25 K. The acceptance angle of the detector determined by the 3.1-mm aperture A5 is 0.2° .

D. Sample manipulator, sample holder, and alignment

The sample manipulator described in Ref. 9 has now been redesigned for high-resolution scattering experiments with fixed rectangular scattering geometry. A high-grade mechanical precision is necessary in particular for recording azimuthal and polar diffraction scans. The task is made harder by temperature constraints: the sample temperature has to be varied in the range 25–1800 K; the scans have to be taken at low and constant surface temperatures; the sample has to be cooled rapidly (a few minutes from 1000 to 25 K).

The sample holder and the sample cooling system have been redesigned completely. The sample crystal now has a cylindrical hat shape: the crystal surface prepared for investigation is ~8 mm in diameter; the diameter of the rear surface is ~11 mm and the crystal thickness is ~2 mm. Figure 2 shows the details of the new sample holder and its mounting to the three rotation axes manipulator. The sample setting (Fig. 2, Nos. 4 and 5) consists of two Mo rings which loosely enclose all but the front face and the central part of the rear face of the hat-shaped Pt crystal (Fig. 2, No. 6). This gives a good thermal contact between Mo rings and Pt crystal. Molybdenum was chosen in order to combine good heat resisting during flash cycles with low heat capacity and

fair heat conductivity for fast cooling of the sample. The expansion coefficients of Pt and Mo are not dramatically different. The crystal is directly heated by electron bombardment (Fig. 2, No. 7). Particular care has to be taken in order to avoid crystal strains at high temperatures. The three screws which hold together the two Mo rings of the setting are therefore tightened very cautiously. In order to keep their positions, the screws are blocked by thin Pd stripes spot welded to the screw heads and sample setting. The height of the outer Mo ring is adapted to the thickness of the respective crystal so that the crystal surface stands out by 0.1–0.2 mm. The inner ring of the sample setting is screwed tightly to another molybdenum ring (Fig. 2, No. 3). The latter is in thermal contact via a copper braid (length 11.5 cm, diameter at the ends 5.5 mm) to the liquid-helium-cooled copper heat exchanger (Fig. 2, No. 2). This braid (Fig. 2, No. 1), treated for ~30 min in a hydrogen atmosphere at 800 °C in order to improve its heat conductivity, is untwisted into seven single cords before mounting, in order to reduce its stiffness. One end is gold brazed to the Mo ring, the other electron beam welded to a copper disk. The latter is screwed via a gold leaf interface to the bottom of the heat exchanger (Fig. 2, No. 2). Care has been taken that all contacting faces are flat and well polished. The Mo ring (Fig. 2, No. 3) is adjusted relative to the inner rotatable bearing ring (Fig. 2, No. 8) by three pushing and three pulling screws, in order to allow for crystal surface orientation. Possible vibrations and strain-induced displacements of the manipulator axis are avoided by fitting the alignment spike (Fig. 2, No. 9) into a horizontally fixed ball bearing.

The two thermocouple wires (Ni–CrNi elements, 0.1 mm in diameter) are spotwelded separately into the step edge of the crystal rim at diametral opposite positions. (The separate welding of the wires avoids noncontrollable thermal gradients between the thermocouple "hot junction" and the Pt crystal.) The wires are then guided radially by insulating tubes through the outer Mo ring to an insulated support on the manipulator shaft. The temperature is stabilized within ± 0.5 K in the low temperature range. The sample can be cooled to 25 K in less than 2 min after flashing up to 1000 K. The average liquid-helium consumption is 2 l/h.

Both the polar and azimuthal angles are varied by step motors. This ensures a continuous and accurate scanning, which is essential when monitoring diffraction patterns. The step motors and the transmission allow an angular resolution of the polar and azimuthal sample rotation of 0.018 and 0.009 deg of arc, respectively. The mechanical accuracy of the azimuthal bearings (carbon-coated molybdenum cage with oxidized steel balls) is determined by the axial and radial play of the cage. The first is minimized by adjusting the two outer shells with three gear rods so that no sticking occurs, the second is given by the workshop accuracy to ± 0.05 mm on the nominal diameter. Both are actually minimized by the pulling force of the stainless-steel string (radial) and the compulsory force of the copper braid (radial and axial). Influence of hysteresis effects on the angular positioning is avoided by always taking the scans in the same direction. The total available angular ranges are 280°, 120°, and 30° for the polar, azimuthal, and tilt motion, respective-

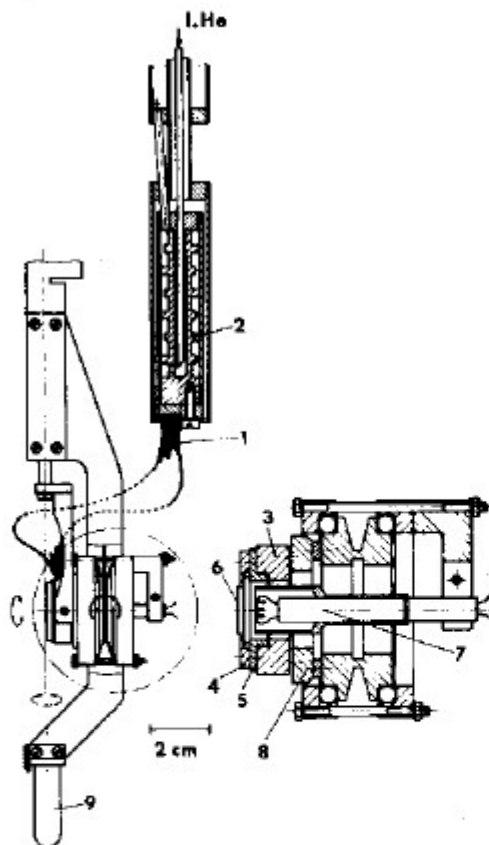


FIG. 2. Manipulator with sample holder and heat exchanger. (1) copper braid; (2) heat exchanger; (3) molybdenum ring; (4,5) molybdenum sample setting; (6) sample; (7) heater filament with Wehnelt cylinder; (8) inner rotatable bearing ring; (9) alignment spike.

ly, with the horizontal tilt axis being 20 mm behind the crystal surface.

The cross point of the generator beam and detector axes is checked in three coordinates with two telescopes (L_1 and L_2), which are focused simultaneously on a thin tip placed at the location of the geometrical sample surface center. The coincidence of the cross point with the tip is optimized by displacements of the apertures, nozzle, and detector. The coincidence of the azimuthal rotation axis with the sample surface normal and of the polar rotation axis with the sample surface diameter are adjusted outside the vacuum system by laser reflection and micrometer control, respectively. After installing the manipulator, the position of the sample surface is aligned successively with each telescope: the polar angle is changed by $\pm 180^\circ$ and the position of the telescope, oriented at a glancing angle with respect to the surface, is verified. The accuracy of the 90° angle between beam generator and detector axes is estimated by laser reflection at the mirrorlike sample surface to be better than $\pm 0.1^\circ$.

E. Time-of-flight unit

As mentioned above we have substantially improved the resolution of the TOF system. As before we use pseudorandom chopping and deconvolute the data by cross correlation.¹⁰

The TOF system consists of a magnetically suspended pseudorandom chopper and, at the end of a 790-mm flight path, of a quadrupole mass analyzer connected to a computer application to measurement and control (CAMAC) multichannel counting unit on line with a PDP-11 computer. The cross-correlation technique has been described previously in detail¹⁰ and compared to the single slot conventional technique.¹²⁻¹⁴ The comparison can be expressed quantitatively by introducing the gain factor $G(f_k)$, which represents the ratio of the variances in channel k and which, for binary shift register sequences, is given by

$$G(f_k) = \frac{\sigma_{\text{single slot}}^2}{\sigma_{\text{pseudorandom}}^2} \simeq \frac{1}{2} \frac{f_k + \bar{u}}{\bar{f} + \bar{u}/n}, \quad (1)$$

where f_k is the number of counts of the time-dependent signal in channel k , \bar{f} is its mean value, \bar{u} is the mean number of counts per channel of the time-independent signal (the real background), and n is the number of slots of the pseudorandom sequence. The pseudorandom chopping has to be preferred when $G(f_k) > 1$. This is always the case when $\bar{u} > 2\bar{f}$ because $n \gg 1$. So far we are only interested in the position, height, and shape of the peaks in the TOF spectra and not in the shape of a, perhaps present, time-dependent background. In this case a much less restrictive condition can be deduced: The pseudorandom chopping has to be preferred when in the "interesting" channels $f_k > 2\bar{f}$, irrespective of the value of \bar{u} . This condition is fulfilled for all significant peaks and thus the pseudorandom chopping is of advantage, even if technically more demanding.

The TOF system used so far, as well as the obvious advantage of the magnetic suspension when the pseudorandom chopper is located in bakeable systems, have been discussed in detail in Ref. 10. The recent improvements are the following:

(i) A new magnetic suspension and drive allowing for rotation frequencies up to 400 s^{-1} has been installed.

(ii) A new CuBe chopper disk ($\phi = 244 \text{ mm}$) with a single binary shift register sequence of length $N = 1023$ with $n = 512$ slots instead of two identical $N = 255$ sequences with 128 slots each, is used. Furthermore the bars separating two subsequent slots have been dropped.

(iii) The commercial multichannel analyzer was replaced by a CAMAC multichannel counting unit. The channel width is therefore no longer limited to $10 \mu\text{s}$. In addition, now each chopper revolution can be used for data accumulation because there is no extra dead time between the last channel of a sweep and the first channel of the subsequent one.

(iv) The flight path is changed from 580 to 790 mm.

The time-scale width of a single slot is $2.5 \mu\text{s}$ at a chopper rotation frequency of 391 s^{-1} . The effective resolution function,¹⁵ which takes into account the finite width of the beam, of the chopper slots and of the channels has a full width at half-maximum (FWHM) of ~ 1.44 times the width of one chopper slot, i.e., $3.6 \mu\text{s}$. Together with the velocity spread of the beam generated by the source ($\sim 0.7\%$ FWHM) and the finite length of the ionization region (estimated to $\sim 5 \text{ mm}$ FWHM) this yields an overall resolution of $8 \mu\text{s}$ FWHM for a typical flight time of $800 \mu\text{s}$ corresponding to 0.42 meV FWHM at 20-meV beam energy. These values agree quite well with the experimentally measured broadening of the TOF peak of the specular and of the diffuse elastic beams. Since the actual photoetched chopper slots do not have exactly the nominal width, the actual sequence (a_i^*) $i = 0, \dots, N-1$ was measured with a laser beam as described in Ref. 10. The actual inverse sequence (b_i^*) $i = 0, \dots, N-1$ is given by

$$\sum_{i=0}^{N-1} b_i^* a_{i-k}^* = \delta_{k0} = \begin{cases} 1 & \text{for } k=0, \\ 0 & \text{for } k=1, \dots, N-1. \end{cases} \quad (2)$$

Since Eq. (2) is a discrete convolution of (b_i^*) with (a_i^*) , a deconvolution program using the discrete Fourier transforms and the convolution theorem yields the actual inverse sequence (b_i^*) in a straightforward way. The calculation of (b_i^*) takes about 8 min on the PDP-11. It has to be repeated only when a new chopper blade is used.

The deconvolution of the (z_k) sequence ($k = 0, \dots, N-1$), i.e., of the counts registered by the CAMAC unit during a TOF measurement, in order to obtain the TOF spectrum (f_k) is performed by cross correlation¹⁰

$$f_k = \sum_{i=0}^{N-1} b_{i-k}^* z_i - \frac{1}{n} \bar{u}. \quad (3)$$

This deconvolution program, which is performed after (and sometimes during) each TOF measurement, takes about 2 min on the PDP-11.

II. MEASUREMENTS AND DISCUSSION

A. TOF measurements

The TOF technique offers a universal scheme of measuring the energy distribution of thermal atoms scattered at a surface; as a result the surface phonon dispersion curves

can be determined. Phonon momentum and energy are obtained from the TOF peak position and incident angle, using conservation of energy and of the momentum component in the surface plane (the vector components in the surface plane are denoted by capitals)

$$\hbar\omega = \hbar^2 k_i^2 / 2m - \hbar^2 k_f^2 / 2m, \quad (4)$$

$$\mathbf{K}_i = \mathbf{K}_f + \mathbf{Q} + \mathbf{G}, \quad (5)$$

where \mathbf{Q} and $\hbar\omega$ are the phonon momentum and energy, respectively, m is the mass of the He atom, \mathbf{k}_i (\mathbf{k}_f) and \mathbf{K}_i (\mathbf{K}_f) are the wave vectors of incident (scattered) He atoms, and \mathbf{G} is a reciprocal-lattice vector.

Figure 3(a) shows a typical TOF spectrum measured from a Pt(111) surface along the $\langle 11\bar{2} \rangle$ direction, with the incident beam angle and energy $\vartheta_i = 35^\circ$ and $E_i = 18.4$ meV, respectively. In Fig. 3(b) the same spectrum is plotted versus the He energy loss ($\Delta E < 0$) and gain ($\Delta E > 0$). The spectrum shows three peaks. The diffuse elastic peak ($\Delta E = 0$) is due to scattering at defects or impurities. The two other peaks are due to single phonon interactions with the vibrational modes of the platinum surface. The energy loss peak at -6.1 meV is attributed to the Rayleigh wave and the loss peak at -7.0 meV to a so-called longitudinal resonance.¹⁶

Another example is given in Fig. 4. The four spectra have been measured under identical scattering conditions ($\vartheta_i = 42^\circ$, $E_i = 18.4$ meV) from Xe films 1, 2, 3 and ~ 25

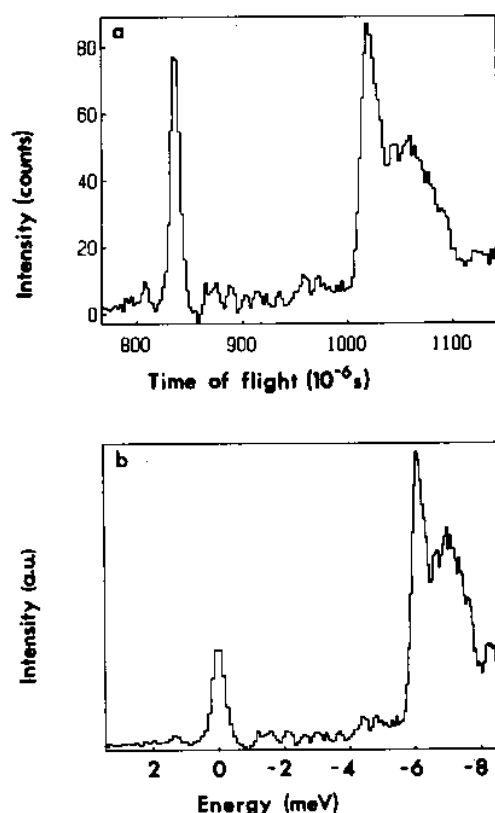


FIG. 3. (a) He TOF spectrum from a clean Pt(111) surface for the $\bar{\Gamma}\bar{M}$ azimuth at a crystal temperature of 150 K, a He beam energy of 18.4 meV and an incident angle $\vartheta_i = 35^\circ$. (b) Same as (a) but transferred to the energy scale; the elastic energy of 18.4 meV is set equal to zero.

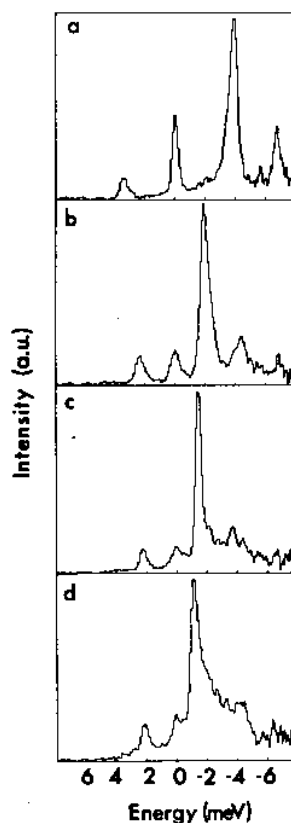


FIG. 4. He TOF spectrum from Xe films on Pt(111) transferred to energy scale; (a) 1 ML, (b) 2 ML, (c) 3 ML, (d) 25 ML. All spectra are taken in the $\bar{\Gamma}\bar{M}$ direction with a beam energy of 18.4 meV, at an incident angle $\vartheta_i = 42^\circ$.

monolayers (ML) thick. By varying the scattering conditions complete phonon dispersion curves for each film have been plotted.¹⁷ The study of the dynamical behavior of physisorbed films is now accessible. As in the case of the Ag(111) substrate,¹⁸ the Xe films on Pt(111) exhibit a gradual evolution from an "Einstein oscillator" behavior of the 1 ML film to the Xe bulk Rayleigh wave behavior of the 25 ML film.

There are two significant features evidenced by the spectra in Fig. 4 which are particularly useful for the investigation of physisorbed films, especially of the type of film growth (wetting versus nonwetting behavior). Due to the high TOF resolution, the different energy losses (gains) of the four films, measured under the same conditions, can be clearly resolved. This makes it possible to straightforwardly determine the completion of each of the first three ML within a few percent. This kind of information is very valuable also in the study of the thermodynamics of physisorbed films. The other feature is the diffuse elastic peak, its intensity being known to be a sensitive measure for the presence of surface defects. In Fig. 4 the diffuse elastic intensity decreases with the film thickness. This decrease is a direct proof for the layer-by-layer growth (complete wetting) of the film.¹⁹ Both types of information are less accessible by other methods and very often a matter of controversy.

B. TOF spectra based *in situ* thermocouple calibration

Accurate and precise temperature measurements in the low-temperature range are a prerequisite for physisorption

studies. Sensors, like silicon diodes, which are commonly used in the low-temperature range because of their large thermoelectric power, are inadequate for sample temperature measurements in surface studies. Indeed, these sensors cannot withstand temperatures of 1000 °C or higher required by the sample surface cleaning procedures. Unfortunately, high-temperature resistant thermocouples have a rather small thermoelectric power in the low-temperature range. For instance, even the Ni-CrNi thermocouple, which we have found to best meet the requirements, has at 25 K a thermoelectric power of only 6 $\mu\text{V/K}$ at an EMF of about - 8.4 meV (with the "cold junction" at 323 K). This asks not only for adequate voltage measurement and control, but also for absolute *in situ* calibration. Indeed, we have noticed that the slight mechanical stress, unavoidable when mounting the thermocouple, leads to changes in the EMF curve corresponding to a few Kelvin in the low-temperature range. Even the calibration performed by immersing the whole crystal holder with mounted thermocouple in liquid nitrogen leads to errors substantially larger than 1 K.

The *in situ* calibration of the thermoelement has been performed via the measurement of the three-dimensional (3D) vapor pressure of a multilayer (bulklike) Xe film grown on a Pt(111) substrate. The procedure takes advantage of two recent observations mentioned in Sec. II A: (a) Xe exhibits complete wetting (i.e., layer-by-layer growth) on Pt(111) down to 25 K; and (b) the energy loss (gains) due to phonon creation (annihilation) in the Xe multilayer can be clearly distinguished from those in the Xe mono-, bi- or trilayers by simple inspection of the high-resolution He TOF spectra.¹⁹ For calibration we proceed as follows. The cleaned crystal is rapidly cooled to a temperature estimated to correspond to a Xe bulk vapor pressure in the range 10^{-6} – 10^{-9} mbar. The EMF of the thermoelement (and thus the Pt crystal temperature) is now maintained constant and the 3D Xe pressure in the chamber is increased step by step. At each step a He TOF spectrum is measured. The appearance of the loss (gain) peak characteristic for Xe multilayers indicates that the vapor pressure of the bulk has been reached. The actual temperature of the substrate is then taken from tabulated vapor pressure isotherms of bulk Xe (Ref. 20); its absolute accuracy is within ± 1 K. The accuracy of the 3D Xe pressure measurement is not very critical: in the accessible pressure range an error of $\pm 20\%$ in pressure reading leads to an absolute calibration error in temperature of only ± 0.2 K.

C. Instrumental peak widths

The shape of the diffraction peaks is determined by both the nonideality of the instrument (nonzero incident beam divergence, detector aperture and spot size, as well as nonideal beam monochromaticity) and the lack of surface perfection (finite domain size, random terrace distributions,

etc.). The pure instrumental peak broadening has been rationalized by correlating it formally with a domain length, the transfer width, which would lead to the same broadening when using an ideal instrument.^{21,22} From the peak broadening measured on real surfaces and by knowing accurately the instrumental broadening, information on the actual domain size can be extracted even for domains substantially larger than the transfer widths.^{22,23} It has been shown further^{24–26} that a detailed analysis of the actual peak shapes supplies, besides accurate average terrace width values, even the actual terrace widths distribution. Such an analysis requires very carefully monitored peak shapes. The constraints imposed in the present apparatus by the He-beam generator and the detector both being immobile lead to characteristic changes of the measured diffraction peak shapes. As shown below, these changes can be accounted for by a straightforward deconvolution. However, the inherent approximations of such a deconvolution procedure make the results of a detailed analysis of the peak shapes less reliable. Accordingly, we will limit ourselves to the deconvolution of the width of the peaks. The estimation of the domain size from the FWHM is accurate enough for usual qualitative discussions.

The He-beam generator and detector being immobile, the azimuthal and the polar scans can be performed only by crystal rotations around the corresponding axes. As stated above this leads to characteristic changes of the measured diffraction peak shapes. This becomes obvious when we consider for instance the specular beam shape in the azimuthal scan: its FWHM is infinite. Indeed, except for some modulations due to bound state resonances, the intensity of the specular beam ($\vartheta_i = \vartheta_f$) is largely constant independent of the crystal azimuth.

Let us consider the question in some detail. The azimuthal FWHM in the case of a "normal" scan, i.e., with the incident plane containing a symmetry axis of the crystal surface and with the detector scanning normal to the incident plane, is

$$\Delta\alpha_n \approx \sqrt{\left(\beta \frac{\sin \vartheta_i}{\sin \vartheta_f}\right)^2 + \left(\beta \frac{l}{L}\right)^2 + \delta^2 + \left(\frac{\lambda_{\text{He}}}{d}\right)^2}, \quad (6)$$

where β is the incident beam divergence, δ is the angle subtended by the detector opening as seen from the crystal, d is the average domain size, λ_{He} is the He wavelength, and l and L are the distances nozzle crystal and crystal detector, respectively. (The second term represents the beam broadening due to the finite spot size.) The nozzle opening being only 5 μm in diameter, the source can be considered as punctual.

If, however, as in the present case and even in all cases when the detector cannot be moved out of the incident plane, the azimuthal FWHM, obtained by rotating the crystal around its normal, becomes

$$\Delta\alpha \approx \sqrt{\left(\beta \frac{\sin \vartheta_i}{\sin \vartheta_f}\right)^2 + \left(\beta \frac{l}{L}\right)^2 + \delta^2 + \left(\frac{\lambda_{\text{He}}}{d}\right)^2} \left| 1 - \frac{\sin \vartheta_i}{\sin \vartheta_f} \right|. \quad (6')$$

For the specular beam ($\vartheta_i = \vartheta_f$), $\Delta\alpha$ obviously diverges. In the case of the present apparatus (fixed scattering angle $\vartheta_d = \vartheta_i + \vartheta_f = 90^\circ$) the azimuthal FWHM is finally

$$\Delta\alpha \approx \sqrt{(\beta \tan \vartheta_i)^2 + \left(\beta \frac{l}{L}\right)^2 + \delta^2 + \left(\frac{\lambda_{\text{He}}}{d}\right)^2} / |1 - \tan \vartheta_i|. \quad (6'')$$

For the polar FWHM similar formulas are obtained. In particular, for the present apparatus, we get

$$\Delta\vartheta = \sqrt{\left[(\beta \cot \vartheta_i)^2 + \left(\beta \frac{l}{L} \tan \vartheta_i\right)^2 + \delta^2 + \left(\frac{\Delta\lambda}{\lambda_{\text{He}}}\right)^2 (1 - \cot \vartheta_i)^2 + \left(\frac{\lambda_{\text{He}}}{d \sin \vartheta_i}\right)^2\right]} / (1 + \cot \vartheta_i), \quad (7)$$

where $\Delta\lambda / \lambda_{\text{He}}$ is the relative wavelength spread of the incident He beam. All parameters in Eqs. (6'') and (7) are accessible to the measurement and thus, in principle, the domain size d can be determined either from an azimuthal [Eq. (6'')] or a polar [Eq. (7)] scan. However, while the "geometrical" spreads β , δ , l , and L can be determined with sufficient accuracy, $\Delta\lambda / \lambda_{\text{He}}$ of a highly monochromatic beam is too small (< 0.01) to be accurately measured even with the high-resolution TOF unit used here. Thus it seems that only the azimuthal scans [Eq. (6'')] are useful for a direct determination of domain sizes. Unfortunately, the orientation of the domains of physisorbed layers might have a certain azimuthal spread, when not well locked on the substrate²⁷ and thus leading to an additional azimuthal broadening of the peaks. A cross-check with polar scans is still necessary.

For the polar scans, Eq. (7) can also be used even without the *a priori* knowledge of $\Delta\lambda / \lambda_{\text{He}}$ from TOF measurements. This is obvious from Eq. (7) if only the specular beam polar profile ($\vartheta_i = 45^\circ$) is exploited. If one wants to also use the FWHM of higher order peaks, $\Delta\lambda / \lambda_{\text{He}}$ can be first determined from the polar FWHM of diffraction peaks measured on a surface with domains much larger than the instrumental transfer width ($d_\infty \gg w_{\text{instrum}}$). The transfer width of the present instrument for the higher order peaks shown in the next paragraph varies around $w_{\text{instrum}} \approx 200 \text{ \AA}$. As a "perfect" surface with $d_\infty \gg w_{\text{instrum}}$ we have used the well-prepared Pt(111) substrate, which was shown to have average terrace widths larger than 2000–3000 \AA .²⁸ The accurate monitoring of the polar shape of the first-order diffraction peak of this surface thus directly supplies the instrumental transfer width and thus a reliable value for $\Delta\lambda / \lambda_{\text{He}}$.

D. Diffraction measurements

The geometrical constraints of the present apparatus affect not only the diffraction peak shape but also the Ewald construction which characterizes the polar scans at constant energy (constant wave vector $|\mathbf{k}_i| = |\mathbf{k}_f| = \text{constant}$). This is illustrated in Fig. 5. The usual polar scan obtained by in-plane rotation of the detector, with the incident beam and the crystal immobile, is represented by the dashed circle segment. The circle has the radius $|\mathbf{k}_f|$ and the center at the

origin of the incident wave vector. One has in this case a whole family of scanning circles, one for each incident angle ϑ_i . The "constrain" scan in the present apparatus is reduced to a single circle segment (solid line) with the radius $\sqrt{k_i^2 + k_f^2} = \sqrt{2}|\mathbf{k}_i|$ centered at the tip of the incident wave vector, i.e., at the (0,0) point on the surface. This limitation restrains to some extent an exhaustive mapping of the resonances, although by varying the incident energy, i.e., $|\mathbf{k}_i|$, a family of solid line circles can also be obtained. On the other hand, the immobility of the detector overcompensates this apparent drawback by allowing for an extremely low background pressure in the detector chamber (multiple differential pumping). The result is illustrated in Fig. 6 where a polar scan from a full Xe monolayer on Pt(111) at 25 K is shown. The three diffraction peaks $(\bar{1}, \bar{1})$, $(\bar{2}, \bar{2})$, and $(\bar{3}, \bar{3})$, which are almost four orders of magnitude smaller than the

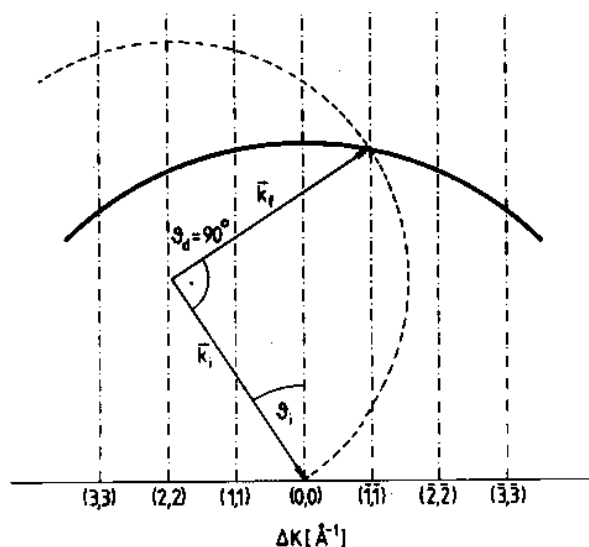


FIG. 5. Ewald diagram for the elastic diffraction of an atom beam at a hexagonal two-dimensional lattice in the \overline{FM} direction for the fixed scattering geometry $\vartheta_d = \vartheta_i + \vartheta_f = 90^\circ$ (solid circle) and for in plane moving detector (dashed circle).

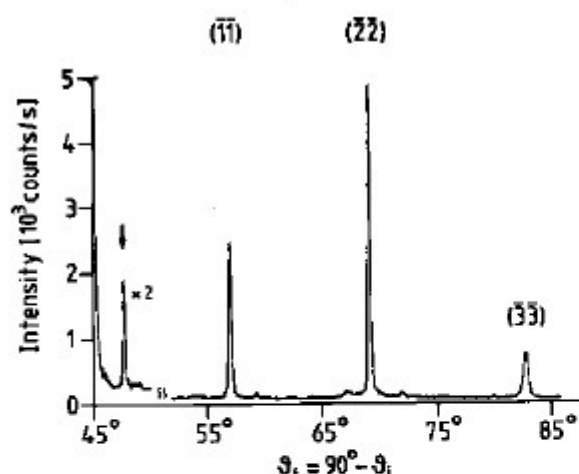


FIG. 6. Polar He diffraction pattern from a complete Xe monolayer on Pt(111) at a surface temperature $T = 25$ K; He beam energy 17.1 meV (see text).

specular beam from the clean Pt(111) surface at the same temperature, are still about hundred times larger than the background. These high-quality plots give confidence in the accuracy of the lattice constant values deduced from the location of the peaks in the polar scans and of the domain size values (see Sec. II C). The azimuthal scan of the $(\bar{2}, \bar{2})$ peak shown in Fig. 7 demonstrates that the Xe layer consists of an approximately equal number of domains rotated by $\pm 3.3^\circ$ with respect to the commensurate $(\sqrt{3} \times \sqrt{3})R30^\circ$ Xe layer observed at lower coverages ($\theta < 0.33$) and at higher temperatures ($62 < T < 99$ K). See Ref. 29 for details. In addition to the three main diffraction peaks in Fig. 6 a sharp peak is present near the specular beam. It belongs to a superstructure, with a large period (23 ± 2 Å) shallow corrugation. The possibility of seeing such faint features is a speciality of He diffraction and originates in the exclusive first-layer sen-

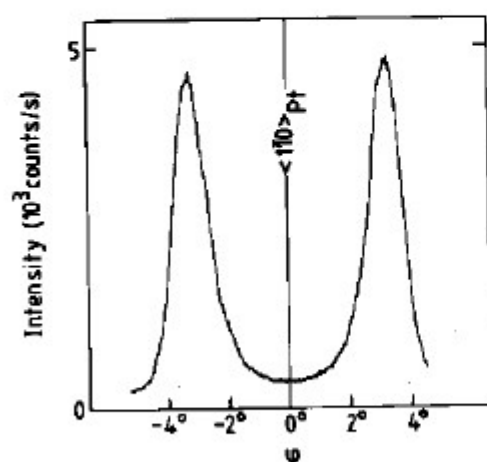


FIG. 7. Azimuthal He diffraction pattern of the $(\bar{2}, \bar{2})$ peak in Fig. 6.

sitivity of thermal scattering.

The last illustration of the capabilities of the apparatus presented here is shown in Fig. 8. It is based on another feature of the He beam, which is of great advantage in ad-layer investigations: the extreme sensitivity of the coherent beams scattered from the substrate for the presence of adatoms. This has been already exploited to investigate the lateral distribution of adsorbates and in particular the 2D condensation of Xe.⁴ Here the measurement of isotherms for thermodynamic studies is shown. The intensity of the specular beam of the Pt(111) substrate (left-hand ordinate) is monitored as a function of the equilibrium 3D Xe pressure at constant surface temperature. The initial slight intensity decrease indicates a small gradual Xe coverage increase. When the 3D Xe condensation pressure is reached the intensity drops nearly three orders of magnitude signaling that the surface is suddenly covered with Xe. In order to uncover the nature of the Xe layer, the experiment is repeated under identical conditions, but with the detector located at the position where the first-order diffraction peak of the commensurate $(\sqrt{3} \times \sqrt{3})R30^\circ$ Xe layer is expected. The monitored intensity (right-hand ordinate) stays constant at background level until the same 3D Xe pressure is reached. At this point the intensity increases abruptly, indicating that the condensed layer is the commensurate one. By repeating the experiments at different equilibrium temperatures the phase diagram of the system can be constructed, with the value of each point cross-checked by the two independent measurements.

III. DISCUSSION

A versatile high-resolution helium scattering apparatus for studying gas surface interactions has been presented. The capabilities of the apparatus for studying surface phonons

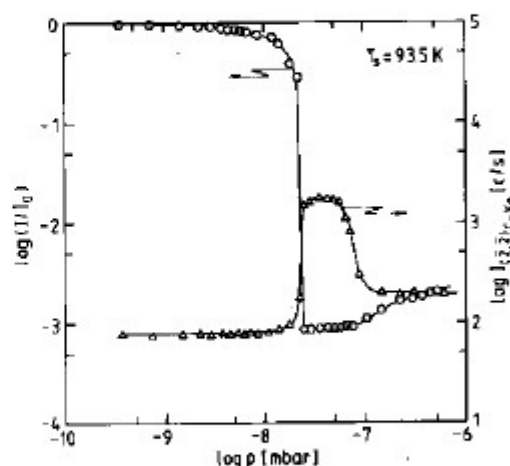


FIG. 8. Adsorption isotherms of Xe on Pt(111). The relative specular He beam peak height $[I/I_0]$ (○) left-hand ordinate with $I_0 \approx 2 \times 10^7$ counts/s and the $(\bar{2}, \bar{2})_{Xe}$ diffraction peak height of the commensurate $(\sqrt{3} \times \sqrt{3})R30^\circ$ layer $[I_{2,2}/I_{c-Xe}]$ (△) right-hand ordinate are plotted vs 3D Xe pressure.

and two-dimensional physisorbed phases have been demonstrated.

In particular, by using high-resolution He scattering in various modes—diffraction, coherent inelastic, and incoherent (diffuse) elastic scattering—this technique allows a *non-destructive*, nearly exhaustive characterization of the thermodynamics, structure and dynamics of physisorbed layers on *arbitrary* substrates.

ACKNOWLEDGMENTS

The authors are indebted to R. L. Palmer for stimulating discussions and his participation in part of the measurements. The building of the CAMAC counting unit by R. Rausch and the magnetic chopper suspension and drive by W. Rubner are gratefully acknowledged. We are also grateful to K. Veltmann for skilled technical assistance and to B. Poelsema for enlightening discussions.

¹F. Knauer and O. Stern, *Z. Phys.* **53**, 779 (1929).

²T. Engel and K. H. Rieder, *Springer Tracts in Modern Physics*, Vol. 91 (Springer, Berlin, 1984).

³J. P. Toennies, *J. Vac. Sci. Technol. A* **2**, 1055 (1984).

⁴G. Comsa and B. Poelsema, *Appl. Phys. A* **38**, 153 (1985).

⁵H. Ibach and T. S. Rahman, *Fifth International Conference on Solid Surfaces*, edited by R. Vanselow and R. Howe, Springer Series in Chemical Physics, Vol. 35 (Springer, Berlin, 1985), p. 455.

⁶*Ordering in Two Dimensions*, edited by S. K. Sinha (North-Holland, Amsterdam, 1980).

⁷*Phase Transitions in Surface Films*, edited by J. G. Dash and J. Ruvalds (Plenum, New York, 1980).

⁸G. Comsa and R. David, *Surf. Sci. Repts.* **5**, 145 (1985).

⁹G. Comsa, R. David, and B. J. Schumacher, *Surf. Sci.* **85**, 45 (1979).

¹⁰G. Comsa, R. David, and B. J. Schumacher, *Rev. Sci. Instrum.* **52**, 789 (1981).

¹¹K. Kern, R. David, and G. Comsa, *Rev. Sci. Instrum.* **56**, 372 (1985).

¹²D. L. Price and K. Sköld, *Nucl. Instrum. Methods* **82**, 208 (1970).

¹³G. Wilhelmi and F. Gompf, *Nucl. Instrum. Methods* **81**, 36 (1970).

¹⁴J. L. Buevoz and G. Roullet, *Rev. Phys. Appl. (Paris)* **12**, 591 (1977).

¹⁵C. V. Nowikow and R. Grice, *J. Phys. E* **12**, 515 (1979).

¹⁶K. Kern, R. David, R. L. Palmer, G. Comsa, and T. S. Rahman, *Phys. Rev. B* **33**, 4334 (1986).

¹⁷K. Kern, R. David, R. L. Palmer, and G. Comsa (unpublished).

¹⁸K. D. Gibson and S. J. Sibener, *Phys. Rev. Lett.* **55**, 1514 (1985).

¹⁹K. Kern, R. David, R. L. Palmer, and G. Comsa, *Phys. Rev. Lett.* **56**, 2823 (1986).

²⁰C. W. Lemig and G. L. Pollack, *Phys. Rev. B* **2**, 3323 (1970).

²¹R. L. Park, J. E. Houston, and D. G. Schreiner, *Rev. Sci. Instrum.* **42**, 60 (1971).

²²G. Comsa, *Surf. Sci.* **81**, 57 (1979).

²³G.-C. Wang and M. G. Lagally, *Surf. Sci.* **81**, 69 (1979).

²⁴L. K. Verheij, J. Lux, and B. Poelsema, *Surf. Sci.* **144**, 385 (1984).

²⁵L. K. Verheij, B. Poelsema, and G. Comsa, *Surf. Sci.* **162**, 858 (1985).

²⁶H. Busch and M. Henzler, *Surf. Sci.* **167**, 534 (1986).

²⁷P. I. Cohen, J. Unguris, and M. B. Webb, *Surf. Sci.* **58**, 429 (1976).

²⁸B. Poelsema, R. L. Palmer, G. Mechttersheimer, and G. Comsa, *Surf. Sci.* **117**, 60 (1982).

²⁹K. Kern, R. David, R. L. Palmer, and G. Comsa, *Phys. Rev. Lett.* **56**, 620 (1986).